CHAPTER 2 DEVELOPMENT OF FINITE ELEMENT MODEL

2.1 INTRODUCTION

In the current research, the behaviour of the jacking pipe and pipe joint are investigated using the finite element method. The finite element program FEPS (Zhou 1997) was mainly used in the research except in Chapter 3 where the program OXFEM (Burd 1996) was used for two-dimensional analysis. FEPS is a finite element package designed to carry out stress analysis with various element types and simple elastic perfectly-plastic material models. The program consists of multiple co-ordinate systems including a cylindrical system which is useful in the current research since pipes are regular structures in this co-ordinate system. The program has various loading input modules especially the non-uniform traction module which can be used to model the non-uniform load at a pipe joint due to pipeline misalignment.

This Chapter describes the development of the finite element model. Mesh generation in the current research is discussed in Section 2.2. Section 2.3 describes the formulation of a two-dimensional interface element and the Mohr-Coulomb frictional model, which play an important role in the research to model the interaction between the concrete pipe and the surrounding soil. A concrete model, modified Matsuoka model, and curved bar elements used to model reinforcements in concrete are discussed in Sections 2.4 and 2.5 respectively. Finally, several solution procedures are presented in Section 2.6.

2.2 MESH GENERATION PROGRAM -- DATAIN

In finite element analysis, the first step is to divide the domain of a structure into many subdomains described as mesh generation. For a simple test example, it is easy to do it by

hand. However, automatic mesh generation is always necessary for complex structures, especially for three-dimensional ones, because of the large amount of data.

Some finite element packages have automatic mesh generation, others use a commercial mesh generation package. In the current research project, the main structures are concrete pipes which are regular structures in a cylindrical co-ordinate system. Furthermore, the stress distributions on some surfaces in a cylindrical co-ordinate system, such as surfaces with r=constant or θ=constant, are usually needed. It may be convenient if the program can deal with a cylindrical system. As a result, a program, DATAIN, was developed for mesh generation in this research. It is simple and effective. A finite element mesh of a pipe with 3375 nodes and 2496 elements is shown in Figure 2.1. The mesh has five different mesh sizes in the θ direction and seven mesh sizes in the z direction. The input data of DATAIN for this mesh is given in Table 2.1. It is clearly seen that the input data is very simple.

2.3 INTERACTION BETWEEN STRUCTURES

To understand the behaviour of the jacking pipe and the pipe joint, one of the main aspects to be investigated is the interaction between the concrete pipe and the surrounding soil, and between the concrete pipe and the packing material. For this purpose, a few two-dimensional interface elements (embedded in three-dimensional continuum) and an interface material model were implemented into the program and are discussed in Sections 2.3.1 and 2.3.2 respectively.

2.3.1 TWO-DIMENSIONAL INTERFACE ELEMENT

The use of interface elements is one of the common methods to study the interaction between structures because it is compatible with other element types and provides a

convenient way to extract the stresses on the interface in the finite element solution (Burd 1986, Beer 1985, Burd and Brocklehurst 1992, Adhikary and Dysin 1998, Ngo-Tran 1996). A two-dimensional interface element is shown in Figure 2.2 with two layers, the upper layer and the lower layer, and four pairs of nodes. Within each pair, the nodes have independent degrees of freedom but share the same co-ordinate position. It should be pointed out that the element formulation described in this section can also easily be used to derive other interface elements with different shapes and different number of nodes, such as a quadrilateral element with 8 pairs of nodes, triangular element with 3 pairs of nodes and triangular element with 6 pairs of nodes. In fact, these interface elements have all been implemented into the program with little extra effort. For simplicity, the interface element with four pairs of nodes is used to demonstrate the element formulation as follows (similar formulations have been used by Beer (1985) and Ngo-Tran (1996)):

The formulation of the element is based on an isoparametric approach. Following the conventional isoparametric approach, the element is mapped into a rectangular element on the isoparametric plane as shown in Figure 2.3. The co-ordinates of a point in the element are related to the nodal co-ordinates by functions of isoparametric co-ordinates ξ and η:

$$\begin{aligned} x &= f_1 x_1 + f_2 x_2 + f_3 x_3 + f_4 x_4 \\ y &= f_1 y_1 + f_2 y_2 + f_3 y_3 + f_4 y_4 \\ z &= f_1 z_1 + f_2 z_2 + f_3 z_4 + f_4 z_4 \end{aligned} \qquad (2.3.1)$$

where x, y and z are co-ordinates at a point in the element, x_i, y_i and z_i are the co-ordinates of the node i. f_i are shape functions defined in isoparametric co-ordinates ξ and η and listed bellow:

$$\begin{aligned} f_1 &= (1 - \xi) (1 - \eta) / 4 \\ f_2 &= (1 + \xi) (1 - \eta) / 4 \\ f_3 &= (1 + \xi) (1 + \eta) / 4 \\ f_4 &= (1 - \xi) (1 + \eta) / 4 \end{aligned} \qquad (2.3.2)$$

The strain increments at a point (ξ, η) within the element are defined as the increments of the relative displacements between the upper layer and the lower layer of the element:

$$d\gamma_1 = du_e^{+} - du_e^{-}$$
$$d\gamma_2 = dv_e^{+} - dv_e^{-} \qquad (2.3.3)$$
$$d\varepsilon_n = dw_n^{+} - dw_n^{-}$$

Where $d\gamma_1$ and $d\gamma_2$ are shear strain increments in the direction of $\mathbf{e}_1$ and $\mathbf{e}_2$, $d\varepsilon_n$ is the normal strain increment in the **n** direction; du_e , dv_e and dw_n are the displacement increments at the point (ξ,η) on the surface in the direction of $\mathbf{e}_1$, $\mathbf{e}_2$ and **n** respectively; and the symbol '+' and '-' denote the upper and lower layer of the element. $\mathbf{e}_1$, $\mathbf{e}_2$ and **n** are unit vectors of a local system as shown in Figure 2.2, which are calculated as follows (Spiegel 1959):

$$\mathbf{e}_1^{*} = \{ \frac{\partial x}{\partial \xi} \quad \frac{\partial y}{\partial \xi} \quad \frac{\partial z}{\partial \xi} \}^{T}$$
$$\mathbf{n}^{*} = \mathbf{e}_1^{*} \times \{ \frac{\partial x}{\partial \eta} \quad \frac{\partial y}{\partial \eta} \quad \frac{\partial z}{\partial \eta} \}^{T}$$
$$\mathbf{e}_1 = \begin{Bmatrix} e_{11} \\ e_{12} \\ e_{13} \end{Bmatrix} = \mathbf{e}_1^{*} / |\mathbf{e}_1^{*}| \qquad (2.3.4)$$
$$\mathbf{n} = \begin{Bmatrix} e_{31} \\ e_{32} \\ e_{33} \end{Bmatrix} = \mathbf{n}^{*} / |\mathbf{n}^{*}|$$
$$\mathbf{e}_2 = \begin{Bmatrix} e_{21} \\ e_{22} \\ e_{23} \end{Bmatrix} = \mathbf{n} \times \mathbf{e}_1$$

Where e_{ij} i,j=1,2,3, are direction cosines of the local system, $|\mathbf{n}^{*}|$ is the norm of the vector $\mathbf{n}^{*}$, T denotes transposition and $\times$ denotes vector cross product operator (Spiegel 1959).

From Figure 2.2, the displacement increments in the direction of $\mathbf{e}_1$, $\mathbf{e}_2$ and **n** at a point (ξ,η) can be related to those in the x, y and z direction at the same point following the conventional displacement transformation between different co-ordinate systems:

$$\begin{Bmatrix} du_e^- \\ dv_e^- \\ dw_n^- \end{Bmatrix} = [\,C\,] \begin{Bmatrix} du^- \\ dv^- \\ dw^- \end{Bmatrix} \tag{2.3.5}$$

Where du_e^-, dv_e^- and dw_n^- are displacement increments at the point (ξ,η) in the direction of $\mathbf{e}_1$, $\mathbf{e}_2$ and $\mathbf{n}$ on the lower layer of the element; du^-, dv^- and dw^- are displacement increments in the x, y and z direction at the same point on the lower layer. The displacement increments on the upper layer have a similar relationship. [C] is the matrix of direction cosines between the global and the local co-ordinate system defined as follow (Spiegel 1959):

$$[\,C\,] = \begin{bmatrix} e_{11} & e_{12} & e_{13} \\ e_{21} & e_{22} & e_{23} \\ e_{31} & e_{32} & e_{33} \end{bmatrix} \tag{2.3.6}$$

In the finite element solution, the final parameters to be solved are the increments of the nodal displacements. So a relationship between the displacement increments at a point and the increments of nodal displacements is needed. The displacement increments on the lower layer in co-ordinate system (x, y, z) at a point are related to the increments of nodal displacements in a similar way as the co-ordinates:

$$\begin{aligned} du^- &= f_1 du_1 + f_2 du_2 + f_3 du_3 + f_4 du_4 \\ dv^- &= f_1 dv_1 + f_2 dv_2 + f_3 dv_3 + f_4 dv_4 \\ dw^- &= f_1 dw_1 + f_2 dw_2 + f_3 dw_3 + f_4 dw_4 \end{aligned} \tag{2.3.7}$$

Where du_i, dv_i and dw_i are the displacement increments at node i in the x, y and z direction. The relationship between the displacement increments at a point and the nodal displacement increments on the upper layer is similar.

Combining equation set (2.3.1) to (2.3.7), a relationship between the strain increments and the increments of the nodal displacements is obtained:

$$\{\, d\varepsilon \,\} = [\, B \,]\, \{\, dU \,\} \tag{2.3.8}$$

Where $\{ dU \} = \{ du_1 \ dv_1 \ dw_1 \ du_2 \ dv_2 \ dw_2 \ \ldots \ du_8 \ dv_8 \ dw_8 \}^T$ is the vector of the increments of the nodal displacements, and $\{ d\varepsilon \} = \{ d\gamma_1 \ d\gamma_2 \ d\varepsilon_n \}^T$ is the vector of strain increments. The geometric matrix $[B]$ is derived as follow:

$$[B] = [C] [-F \ \ F] \tag{2.3.9}$$

$$[F] = \begin{bmatrix} f_1 & 0 & 0 & f_2 & 0 & 0 & & f_4 & 0 & 0 \\ 0 & f_1 & 0 & 0 & f_2 & 0 & \ldots & 0 & f_4 & 0 \\ 0 & 0 & f_1 & 0 & 0 & f_2 & & 0 & 0 & f_4 \end{bmatrix} \tag{2.3.10}$$

The element stiffness matrix is obtained by following the conventional approach (Zienkiewicz 1977):

$$\begin{aligned} [K] &= \iint_S [B]^T [D] [B] \, ds \\ &= \int_{-1}^{1} \int_{-1}^{1} [B]^T [D] [B] \, J \, d\xi \, d\eta \end{aligned} \tag{2.3.11}$$

Where $[K]$ is the element stiffness matrix; S is the element domain and $[D]$ is the material matrix which is discussed in detail in Section 2.3.2. $J = | \mathbf{n}^* |$ is the Jacobian determinant of co-ordinates transformation between the global co-ordinate system (x, y, z) and the isoparametric co-ordinate system (ξ, η).

2.3.2 THE MOHR-COULOMB FRICTIONAL MODEL

For the interface element discussed in Section 2.3.1, the stress increments are assumed to be related linearly to the strain increments within the element when the interface is elastic (Goodman et al. 1968, Burd 1986, Beer 1985, Burd and Brocklehurst 1992, Ngo-Tran 1996) and the constitutive equation is:

$$\{ d\sigma \} = [D] \{ d\varepsilon \} \tag{2.3.12}$$

Where $\{ d\sigma \} = \{ d\tau_1 \;\; d\tau_2 \;\; d\sigma_n \}^T$ is the vector of stress increments in the direction of $\mathbf{e}_1$, $\mathbf{e}_2$ and $\mathbf{n}$; $\{ d\varepsilon \}$ is the vector of strain increments defined in Section 2.3.1 and $[D]$ is the elastic material matrix defined as follows:

$$[D] = \begin{bmatrix} K_s & 0 & 0 \\ 0 & K_s & 0 \\ 0 & 0 & K_n \end{bmatrix} \tag{2.3.13}$$

K_n and K_s are the normal stiffness and the shear stiffness of the interface. Here the shear stiffness is assumed to be the same in both $\mathbf{e}_1$ and $\mathbf{e}_2$ direction.

As in most elastic-plastic problems, the interface is assumed to yield when the stresses satisfy the Mohr-Coulomb criterion:

$$\begin{aligned} f &= \tau^2 - (c - \sigma_n \tan\varphi)^2 \\ &= (\tau_1^2 + \tau_2^2) - (c - \sigma_n \tan\varphi)^2 = 0 \end{aligned} \tag{2.3.14}$$

Where f is the yield function; σ_n, τ, τ_1 and τ_2 are the normal stress, total shear stress, shear stress in the $\mathbf{e}_1$ and $\mathbf{e}_2$ direction; c and φ are the cohesion and the angle of friction assigned to the interface. For the case of plastic material behaviour, the plastic strain increments are derived from a plastic potential which is assumed to have a similar form as the yield function:

$$\{ d\varepsilon_p \} = \lambda \left\{ \frac{\partial g}{\partial \sigma} \right\} \tag{2.3.15}$$

$$\begin{aligned} g &= \tau^2 - (c_1 - \sigma_n \tan\psi)^2 \\ &= (\tau_1^2 + \tau_2^2) - (c_1 - \sigma_n \tan\psi)^2 \end{aligned} \tag{2.3.16}$$

Where $\{ d\varepsilon_p \}$ is the vector of the plastic strain increments; λ is a factor of proportionality determined by the consistency condition; g is plastic potential; ψ is the dilation angle assigned to the interface and the cohesion parameter $c_1 = c + \sigma_n (\tan\psi - \tan\varphi)$ is obtained by setting $f = g$ at the current stress state as shown in Figure 2.4.

The constitutive equation between the stress increments and the strain increments can be obtained by following the conventional procedure (Zienkiewicz 1977) as in most elastic-plastic problems:

$$\{ d\sigma \} = [D_{ep}] \{ d\varepsilon \} \tag{2.3.17}$$

Where $[D_{ep}]$ is the elastic-plastic material matrix derived as following:

$$\left[D_{ep}\right] = [D] - \frac{[D]\left\{\frac{\partial g}{\partial \sigma}\right\}\left\{\frac{\partial f}{\partial \sigma}\right\}^T [D]}{\left\{\frac{\partial f}{\partial \sigma}\right\}^T [D]\left\{\frac{\partial g}{\partial \sigma}\right\}} \tag{2.3.18}$$

$$\left\{\frac{\partial f}{\partial \sigma}\right\}^T = \{ \tau_1 \quad \tau_2 \quad (c - \sigma_n \tan\varphi) \tan\varphi \} \tag{2.3.19}$$

$$\left\{\frac{\partial g}{\partial \sigma}\right\}^T = \{ \tau_1 \quad \tau_2 \quad (c_1 - \sigma_n \tan\psi) \tan\psi \} \tag{2.3.20}$$

2.3.3 UPDATE OF DISPLACEMENTS, STRAINS AND STRESSES

In elastic-plastic problems, a finite element solution is usually obtained step-by-step using an incremental method. The increments of the nodal displacements are solved in each step and then the nodal displacements, strains and stresses are updated as following:

$$\begin{aligned} &\{ U \} = \{U_0\} + \{ dU \} \\ &\{ d\varepsilon \} = [B] \{ dU \} \\ &\{\varepsilon\} = \{\varepsilon_0\} + \{ d\varepsilon \} \\ &\{ d\sigma \} = \int \left[D_{ep} \right] d\varepsilon \\ &\{\sigma\} = \{\sigma_0\} + \{ d\sigma \} \end{aligned} \tag{2.3.21}$$

Where $\{ U \}$, $\{U_0\}$ and $\{ dU \}$ are the current nodal displacements, the nodal displacement at end of previous step and the increments of nodal displacements in the current step; $\{\varepsilon\}$, $\{\varepsilon_0\}$

and $\{d\varepsilon\}$ are the current strains, the strains at end of previous step and the increments of strains in the current step; $\{\sigma\}$ and $\{\sigma_0\}$ are the current stresses and the stresses at end of previous step. $\{d\sigma\}$ is the increments of stresses in the current step, which is obtained by numerical integration in analysis (Burd 1986).

If the stress state is still elastic (that is $f < 0$), the calculation moves to the next step. As in most elastic-plastic models, if the stress state is in the plastic zone ($c - \sigma_n \tan\varphi > 0$ and $f \geq 0$), the stresses should be projected back on the initial yield surface as shown in Figure 2.5 because the model discussed here is an elastic perfectly-frictional model (no hardening effect). To project the stresses back on the yield surface, many return algorithms have been developed (Simo and Taylor 1985, Krieg and Krieg 1977, Schreyer et al 1979, Ortiz et al 1983, Oritiz and Simo 1986). The closest point projection algorithm (Burd 1986) is adopted in the current research, in which the return direction is always normal to the yield surface.

In the current research, the concrete pipe can separate from the surrounding soil or from the packing material due to pipeline misalignment. The gap plays an important role in the pipe performance because the gap changes the stress distribution significantly in its adjacent region. In order to take the influence of the gap into consideration, the interface model here consists of a gap zone ($c - \sigma_n \tan\varphi \leq 0$) as shown in Figure 2.5. Whenever the stress state at a point enters into this gap zone, it is assumed that the two layers of the interface element separate at this point and a gap exists between them. Then the stresses and the stiffness of the element at this point are set to zero according to the nature of the gap (for the purpose of numerical stability , the stiffness is set to a very small value in analysis). In the current research, loading is applied monotonically; so there is no global unloading. However, the gap can be closed ($\varepsilon_n \leq 0$) due to local unloading. When the gap is closed, the element stiffness at this point recovers completely at once and the stresses are updated as follows:

$$\varepsilon_n = \varepsilon_{n0} + d\varepsilon_n$$

$$t = \varepsilon_n / d\varepsilon_n \qquad (2.3.22)$$

$$\{ d\sigma \} = t [D] \{ d\varepsilon \}$$

$$\{\sigma\} = \{\sigma_0\} + \{ d\sigma \} = \{d\sigma\}$$

Where ε_n, ε_{n0} and $d\varepsilon_n$ are the normal strain, the normal strain at end of previous step and the increment of the normal strain in the current step as defined in Section 2.3.1; t is the proportional time after the gap is closed within the step, that is, $\varepsilon_{n0} + (1- t) d\varepsilon_n = 0$. The total stresses are equal to the increments of the stress because the stresses at the end of previous step $\{\sigma_0\}$ are zero within the gap.

2.3.4 EXAMPLE ANALYSIS

After implementing the interface element and the interface model into the program, two examples have been analysed to verify the program. The first example is shown in Figure 2.6 with two very stiff blocks and an interface between them. Just one 8-node brick element is used for each block and one quadrilateral interface element with four pairs of nodes for the interface. In order to examine the behaviour of the interface, the two blocks are considered as rigid with a high Young's modulus E = 10^{11}MPa and a zero Poisson's ratio $\mu = 0$. For the interface, the material constants are assigned with a normal stiffness K_n = 2000MPa /mm, a shear stiffness K_s = 1000MPa /mm, a friction angle $\varphi = 26.57^0$, a dilation angle $\psi = 26.57^0$ and a zero cohesion parameter c = 0. The lower block is fixed at the bottom. In the analysis, a uniform vertical displacement δ_1 = -0.1mm was first applied at the top of the upper block, then another uniform displacement δ_2 = 0.2mm was applied on the left surface of the upper block as shown in the figure. The analysis was carried out using the modified Euler iteration scheme (Burd 1986). One step was used for the first calculation stage with the given displacement at the top since the interface was in an elastic state and 100 steps were used in the second stage with the given displacement on the left surface. The results are shown in Figure 2.7.

From the figure, it is clear that at end of the first stage (point A in Figure 2.7) the stresses are linearly related to the given displacement ($\sigma_n = K_n \delta_1$). When the displacement δ_2 was applied on the left surface of the top block, the shear stress increases linearly step by step with a constant normal stress until the theoretical yield point B and then the stresses increase along the yield surface as would be expected.

Another example with two quadrilateral interface elements is shown in Figure 2.8 to examine the gap behaviour of the interface. The two blocks are again considered as rigid with the same material constants used in the first example and two brick elements were used for each block in the analysis. The lower block is also fixed at the bottom. The material constants of the interface are the same as those in the first example. In this example, a linearly distributed vertical displacement was first applied on the top of the upper block to form a gap at the left side of the interface, then an uniform displacement was applied to the top to close the gap. The analysis was again carried out using a modified Euler iteration procedure. There were 200 steps for both the first and the second calculation stage. The stresses at the Gauss point A, B, C and D on the interface are shown in Figure 2.9.

Figure 2.9 shows that in the calculation stage one, the stresses at point A and B are zero because there is a gap between the two blocks and that the normal stresses at point C and D increase linearly with the applied displacement but at different rates since the applied displacement is different at point C and D. In the second calculation stage, the normal stresses at point C and D increase with the applied uniform displacement at the same rate. The normal stress at point B is zero at first and then increases linearly with the given displacement after the gap at this point is closed. The gap at point A is closed at a late stage, so the normal stress at this point is zero for most of the calculation. For this simple example, a closed form solution of the stresses on the interface can be obtained, that is, $\tau = 0$, $\sigma_n = K_n \varepsilon_n$ when $\varepsilon_n < 0$ and $\sigma_n = 0$ when $\varepsilon_n > 0$. Clearly, the numerical results in Figure 2.9

are the same as the closed form solution. This means that the interface element and the interface model have successfully been implemented into the program.

2.4 NUMERICAL MODEL OF CONCRETE

2.4.1 LITERATURE REVIEW

Concrete is a complex composite material mainly used to undertake compressive load. The behaviour of concrete is complex. Experimental tests show that concrete behaves in a non-linear manner (Jiang and Feng 1991, Neville 1981). Figure 2.10 shows a typical stress-strain relationship of concrete under uniaxial load. In the compression region, several numerical models have been developed to express this curve. One of them proposed by Hognestad (Bangash 1989) is as follows:

$$\frac{\sigma}{f_c} = 2\frac{\varepsilon}{\varepsilon_0}\left(1 - \frac{\varepsilon}{\varepsilon_0}\right) \qquad \text{for } 0 < \varepsilon < \varepsilon_0$$

$$\frac{\sigma}{f_c} = 1 - \left(\frac{\varepsilon - \varepsilon_0}{\varepsilon_c - \varepsilon_0}\right) \qquad \text{for } \varepsilon_0 < \varepsilon < \varepsilon_c \qquad (2.4.1)$$

Where σ and ε are stress and strain respectively, f_c is the compressive strength, ε_0 is the strain at peak compressive stress f_c, and ε_c is the ultimate strain. In the tension region, the strain-stress relationship can approximately be expressed by a bi-linear line.

For the behaviour of concrete under biaxial stress, much research work has been done. Numerous formulations on the constitutive relations have been developed (Kupfer and Gerstle 1973, Chen and Chen 1975, Neville 1981) The expressions are generally divided into different regions, say compression-compression, tension-compression and tension-tension region. Most of the formulations are similar with some deviations in the region near the equal biaxial compressive stress state. A typical biaxial stress interaction curve is shown in Figure 2.11. It can be seen from the figure that biaxial tensile strength is no different from uniaxial

tensile strength; under biaxial compression, the compression strength for σ_1 increases with the compressive stress σ_3 and reaches its maximum at about $\sigma_3 / \sigma_1 = 0.5$; and in the tension-compression region, the tensile (compressive) strength decreases approximately linearly when the compressive (tensile) stress increases.

However, there are many examples in the design of concrete when a satisfactory explanation of the ultimate strength behaviour can only be achieved if the concrete is considered to be subjected to a three-dimensional stress state. To treat these problems, many models have been developed in the three-dimensional stress state from the simple one-parameter model to very the complicated eight-parameter model, such as Boswell and Chen (1987), de Boer and Dresenkamp (1989). One typical three-dimensional concrete model is shown in Figure 2.12. Other commonly used models include Mohr-Coulomb model, Drucker-Prager model, William three-parameter model, Ottoson model and William five parameter model (Jiang and Feng 1991).

After the discussion above, it is known that the numerical model for concrete is usually complex in order to model the behaviour of concrete properly. However, some important properties of concrete may be stated as following:

(1) Tensile strength is much weaker than compressive strength by about $\frac{1}{8}$ to $\frac{1}{14}$.

(2) Concrete has limited ductility at both tension and compression failure, i.e., concrete will either crush or crack instead of flowing after reaching failure.

(3) The stress-strain relationship is generally non-linear. However, when the stress is below 40-60% of the ultimate stress, the relationship is almost linear elastic.

(4) Hydrostatic pressure has significant influence on discontinuity and failure of concrete.

(5) The failure curve of stress is a smooth non-circular closed curve in the deviatoric plane and changes from nearly triangular to nearly circular with increasing hydrostatic pressure.

2.4.2 FORMULATION OF THE MODIFIED MATSUOKA MODEL

One of the successful soil models, the Matsuoka model (Matsuoka 1976, Burd 1986), is modified here to include tensile strength in order to simulate concrete under compression. This model has the advantage that it is simple and there is no singularity on its yield surface except the origin, and that its parameters have engineering significance and are easily measured. The modified model is also used to model soils with cohesion in this research.

The modified Matsuoka model is illustrated in Figure 2.13 and its yield function can be written as (Matsuoka 1976, Burd 1986):

$$f = I_3^* \zeta - I_1^* I_2^* \tag{2.4.2}$$

$$\zeta = 9 + 8 \tan\varphi \tag{2.4.3}$$

Where the parameter φ is the frictional angle and I_i^* are defined as follows:

$$\begin{aligned} I_1^* &= \sigma_1^* + \sigma_2^* + \sigma_3^* \\ &= \sigma_x^* + \sigma_y^* + \sigma_z^* \\ I_2^* &= \sigma_1^* \sigma_2^* + \sigma_2^* \sigma_3^* + \sigma_1^* \sigma_3^* \\ &= \sigma_x^* \sigma_y^* + \sigma_y^* \sigma_z^* + \sigma_x^* \sigma_z^* + \tau_{xy}^2 + \tau_{xz}^2 + \tau_{yz}^2 \\ I_3^* &= \sigma_1^* \sigma_2^* \sigma_3^* \\ &= \sigma_x^* \sigma_y^* \sigma_z^* + 2\,\tau_{xy}\tau_{xz}\tau_{yz} - \sigma_x^* \tau_{yz}^2 - \sigma_y^* \tau_{xz}^2 - \sigma_z^* \tau_{xy}^2 \\ \sigma_i^* &= \sigma_i + M \quad i=1, 2, 3, x, y, z \end{aligned} \tag{2.4.4}$$

σ_1 etc. are principal stresses and σ_x, τ_{xy} etc. are the conventional stresses defined in Cartesian co-ordinate system (Timoshenko and Goodier 1970). M is a material constant which can be derived from the uniaxial tensile strength f_t or from the cohesion parameter c as shown in Figure 2.13(b) by assuming that under uniaxial tension a material reaches its tensile strength and its shear strength at the same time:

$$\begin{aligned} M &= c / \tan\varphi \\ &= \frac{f_t}{2}\left(1 + \frac{1}{\sin\varphi}\right) \end{aligned} \tag{2.4.5}$$

The plastic potential of this model is assumed to have the same form of the yield function but with different material parameters:

$$g = J_3^* \zeta^* - J_1^* J_2^* \tag{2.4.6}$$

$$\zeta^* = 9 + 8 \tan\psi \tag{2.4.7}$$

Where ψ is the dilation angle of the model and similarly J_i^* are defined as follows:

$$\begin{aligned}
J_1^* &= \overline{\sigma_1} + \overline{\sigma_2} + \overline{\sigma_3} \\
&= \overline{\sigma_x} + \overline{\sigma_y} + \overline{\sigma_z} \\
J_2^* &= \overline{\sigma_1}\,\overline{\sigma_2} + \overline{\sigma_2}\,\overline{\sigma_3} + \overline{\sigma_1}\,\overline{\sigma_3} \\
&= \overline{\sigma_x}\,\overline{\sigma_y} + \overline{\sigma_y}\,\overline{\sigma_z} + \overline{\sigma_x}\,\overline{\sigma_z} + \tau_{xy}^2 + \tau_{xz}^2 + \tau_{yz}^2 \\
J_3^* &= \overline{\sigma_1}\,\overline{\sigma_2}\,\overline{\sigma_3} \\
&= \overline{\sigma_x}\,\overline{\sigma_y}\,\overline{\sigma_z} + 2\,\tau_{xy}\tau_{xz}\tau_{yz} - \overline{\sigma_x}\,\tau_{yz}^2 - \overline{\sigma_y}\,\tau_{xz}^2 - \overline{\sigma_z}\,\tau_{xy}^2 \\
\overline{\sigma_i} &= \sigma_i + M^* \qquad i=1, 2, 3, x, y, z
\end{aligned} \tag{2.4.8}$$

The parameter M^* is determined by setting $f = g$ at the current stress state as shown in Figure 2.13(b).

Under elastic stress state, the constitutive equation is the usual elastic material matrix:

$$\{ d\sigma \} = [D] \{ d\varepsilon \} \tag{2.4.9}$$

Where $\{ d\sigma \} = \{ d\sigma_x \; d\sigma_y \; d\sigma_z \; d\tau_{yz} \; d\tau_{xz} \; d\tau_{xy} \}^T$ and $\{ d\varepsilon \} = \{ d\varepsilon_x \; d\varepsilon_y \; d\varepsilon_z \; d\gamma_{yz} \; d\gamma_{xz} \; d\gamma_{xy} \}^T$ are the vector of the stress increments and the vector of the strain increments. $[D]$ is the elastic material matrix defined as:

$$[D] = \frac{E(1-\mu)}{(1+\mu)(1-2\mu)} \begin{bmatrix} 1 & \frac{\mu}{1-\mu} & \frac{\mu}{1-\mu} & 0 & 0 & 0 \\ \frac{\mu}{1-\mu} & 1 & \frac{\mu}{1-\mu} & 0 & 0 & 0 \\ \frac{\mu}{1-\mu} & \frac{\mu}{1-\mu} & 1 & 0 & 0 & 0 \\ 0 & 0 & 0 & \frac{1-2\mu}{2(1-\mu)} & 0 & 0 \\ 0 & 0 & 0 & 0 & \frac{1-2\mu}{2(1-\mu)} & 0 \\ 0 & 0 & 0 & 0 & 0 & \frac{1-2\mu}{2(1-\mu)} \end{bmatrix} \qquad (2.4.10)$$

Where E and μ are Young's modulus and Poisson's ratio of a material.

When the stress state is plastic, an elastic-plastic material matrix can be obtained following the similar procedure in Section 2.3.2 for the interface model. Again, equation (2.3.18) is used to obtain the elastic-plastic material matrix [D_{ep}] with [D] defined in equation (2.4.10) and $\left\{\frac{\partial f}{\partial \sigma}\right\}$, $\left\{\frac{\partial g}{\partial \sigma}\right\}$ defined as follows:

$$\left\{\frac{\partial f}{\partial \sigma}\right\} = \begin{Bmatrix} \varsigma(\sigma_y^* \sigma_z^* - \tau_{yz}^2) - I_1^*(\sigma_y^* + \sigma_z^*) - I_2^* \\ \varsigma(\sigma_x^* \sigma_z^* - \tau_{xz}^2) - I_1^*(\sigma_x^* + \sigma_z^*) - I_2^* \\ \varsigma(\sigma_x^* \sigma_y^* - \tau_{xy}^2) - I_1^*(\sigma_x^* + \sigma_y^*) - I_2^* \\ 2\varsigma(\tau_{xz}\tau_{xy} - \sigma_x^* \tau_{yz}) + 2\tau_{yz} I_1^* \\ 2\varsigma(\tau_{xy}\tau_{yz} - \sigma_y^* \tau_{xz}) + 2\tau_{xz} I_1^* \\ 2\varsigma(\tau_{yz}\tau_{xz} - \sigma_z^* \tau_{xy}) + 2\tau_{xy} I_1^* \end{Bmatrix} \qquad (2.4.11)$$

$$\left\{\frac{\partial g}{\partial \sigma}\right\} = \begin{Bmatrix} \varsigma^* (\overline{\sigma_y}\,\overline{\sigma_z} - \tau_{yz}^2) - J_1^* (\overline{\sigma_y} + \overline{\sigma_z}) - J_2^* \\ \varsigma^* (\overline{\sigma_x}\,\overline{\sigma_z} - \tau_{xz}^2) - J_1^* (\overline{\sigma_x} + \overline{\sigma_z}) - J_2^* \\ \varsigma^* (\overline{\sigma_x}\,\overline{\sigma_y} - \tau_{xy}^2) - J_1^* (\overline{\sigma_x} + \overline{\sigma_y}) - J_2^* \\ 2\varsigma^* (\tau_{xz}\tau_{xy} - \overline{\sigma_x}\tau_{yz}) + 2\tau_{yz} J_1^* \\ 2\varsigma^* (\tau_{xy}\tau_{yz} - \overline{\sigma_y}\tau_{xz}) + 2\tau_{xz} J_1^* \\ 2\varsigma^* (\tau_{yz}\tau_{xz} - \overline{\sigma_z}\tau_{xy}) + 2\tau_{xy} J_1^* \end{Bmatrix} \qquad (2.4.12)$$

The element stiffness matrix can be calculated in the similar way as that of the interface element in Section 2.3.

For updating the displacements, strains and stresses, the approach discussed in Section 2.3.3 is also used in this model. When the stress state is in the plastic zone, the stresses are projected back on the yield surface using the closest point projection algorithm (Burd 1986, Simo and Taylor 1985, Krieg and Krieg 1977). When the stress state enters the crack zone (the most tensile principal stress $\sigma_1 \geq M$) as shown in Figure 2.13(b), the stresses are proportionally put back to the yield surface to avoid singularity in calculation. This means that the modified Matsuoka model cannot simulate crack behaviour of a material. To deal with cracking, a more complex material model is needed, which is out of the scope of the current research.

2.4.3 EXAMPLE ANALYSIS

An example has been analysed to verify the implementation of the modified Matsuoka model. The example is a block with four elements as shown in Figure 2.14. The block is simply supported at the bottom. The material constants are the Young's modulus E = 10GPa, Poisson's ratio μ = 0.2, friction angle $\varphi = 26.57^0$, dilation angle $\psi = 26.57^0$ and uniaxial tensile strength f_t = 6MPa. Two cases have been examined. In the first case, a uniform displacement is applied at the top of the block as shown in Figure 2.14. The analysis was

carried out with modified Euler iteration scheme and 200 steps were used. The results are shown in Figure 2.15(a). The figure shows that the magnitude of the stress σ_z increases linearly with the applied displacement until the theoretical compression yield limit (-15.71MPa) at point A. Afterwards the stress takes a constant value of the yield limit except a small deviation in the region of point A. This means that the numerical results are almost the same as the theoretical solution except for a small disturbance in the region of the yield point A.

In the second case, another uniform displacement is applied on the top but in the opposite direction as shown in the figure. The results are shown in Figure 2.15(b). Again the magnitude of the stress σ_z increases linearly with the applied displacement until the theoretical tensile yield limit (that is, the uniaxial tensile strength 6MPa) at point B. After the yield point, the stress is constant (6MPa) since the model includes neither any hardening parameter nor cracking behaviour. Again, the numerical results are the same as the theoretical solution for this simple example. The results from this example suggest that the modified Matsuoka model has correctly been implemented in the program and works well.

2.5 NUMERICAL MODEL OF REINFORCEMENT

The model discussed in Section 2.4 is for plain concrete under compression. Due to low concrete tensile strength, cracking usually exists in the tension region within concrete structures. To increase the tensile strength of concrete structures, reinforcements are usually used. With cracking in the tension region and with reinforcements, the behaviour of the concrete is different and more complicated. However, as pointed out in Chapter 1, the research in this project is focused on the pipe behaviour under working conditions. The complex cracking behaviour of concrete is out of the scope of this thesis.

In this Section, first, a brief literature review about cracking and reinforcements in concrete is presented. Then a formulation of curved bar elements used as reinforcements is discussed. Finally, two validating examples of the bar elements are presented.

2.5.1 LITERATURE REVIEW

To treat the crack, two distinct models, the discrete-cracking model and the smeared-cracking model, have been developed. The smeared-cracking model treats cracking as distributed cracks on the continuum level. Since this model does not require the knowledge of a crack direction in advance nor the change of topology of an element mesh, it is more commonly used nowadays (Vidosa al et 1991a and 1991b, Morcos and Jorhovde 1992). One of the simple procedures for the smeared-cracking model is to let the strength in direction of maximum stress vanish suddenly at the detection of a crack. Bazant (1976) pointed out that this simple model introduces a fictitious dependence on the size of finite element meshes. Afterwards, many more accurate models have been developed by introducing the concept of linear fracture mechanics (Bazant and Cedolin 1979), or by introducing non-linear mechanics concepts (Hillerborg et at 1976, Yamaguchi and Chen 1990).

The steel reinforcement in concrete is usually considered uniformly distributed within the element with uniaxial stiffness following the bar direction. Moreover, to obtain the constitutive law (one local co-ordinate should be in the bar direction), the strain increments in the reinforcement are usually assumed to be the same as those in the concrete and the stress increments are assumed to be the sum of the stress increments in the concrete and in the reinforcement (Owen et al 1983, Lin and Scordelis 1975). The behaviour of the reinforced concrete with cracks is derived by combining the reinforcement constitutive law and the smeared-cracking model (Frantzeskakis and Theillout 1989, Bazant and Gambarova 1980, Bazant and Tsubaki 1980).

Another method to model the reinforcement is to take the concrete and the reinforcement as two different materials. The bond between the concrete and the reinforcement is considered to be perfect. In analysis, the reinforcement is treated as a separate bar element carrying only axial stress. The volume of the bar may be ignored when dealing with the concrete. The bar elements will be put at an appropriate position or even embedded within the concrete element (Phillips 1987, Damjanic et al 1987). This way is simple and effective when the amount of reinforcement is small. This method is adopted in this project for the back analysis of the experiment with local steel reinforcements.

2.5.2 CURVED BAR ELEMENTS

A bar element with n nodes is shown in Figure 2.16. The formulation procedure is again based on an isoparametric approach. The element is first mapped into a isoparametric plane as a one-dimensional straight line as shown in Figure 2.17. The co-ordinates at a point in the element are related to nodal co-ordinates as functions of the isoparametric co-ordinate ξ in a similar way as those in the interface element in Section 2.3.1:

$$\begin{aligned} x &= f_1 x_1 + f_2 x_2 \quad \ldots \quad + f_n x_n \\ y &= f_1 y_1 + f_2 y_2 \quad \ldots \quad + f_n y_n \\ z &= f_1 z_1 + f_2 z_2 \quad \ldots \quad + f_n z_n \end{aligned} \tag{2.5.1}$$

Where x, y, z are the co-ordinates at a point within the element; x_i, y_i and z_i are the co-ordinates of node i. f_i, i=1, ... n, are the shape functions defined as follows:

$$f_i = \frac{(\xi - 0) \ldots (\xi - \frac{i-1}{n-1})(\xi - \frac{i+1}{n-1}) \ldots (\xi - 1)}{(\frac{i}{n-1} - 0) \ldots (\frac{i}{n-1} - \frac{i-1}{n-1})(\frac{i}{n-1} - \frac{i+1}{n-1}) \ldots (\frac{i}{n-1} - 1)} \tag{2.5.2}$$

The displacement increments at a point in the element are derived from the increments of nodal displacement in a similar way as the co-ordinates:

$$du = f_1 du_1 + f_2 du_2 \ \ldots \ + f_n du_n$$
$$dv = f_1 dv_1 + f_2 dv_2 \ \ldots \ + f_n dv_n \qquad (2.5.3)$$
$$dw = f_1 dw_1 + f_2 dw_2 \ \ldots \ + f_n dw_n$$

Where du, dv and dw are the displacement increments at a point within the element; du_i, dv_i and dw_i are the increments of the nodal displacements.

The bar element has only axial strain and bears axial force. From Figure 2.16, the axial strain increment at a point within the element can be derived by (Spiegel 1959):

$$d\varepsilon = \frac{\partial u_\xi}{\partial s} = \frac{\partial u_\xi}{\partial \xi}\frac{\partial \xi}{\partial s} \qquad (2.5.4)$$

Where $d\varepsilon$ is the axial strain increment; u_ξ is the displacement in the $\mathbf{e}_1$ direction at the point; s is the length between the point 1 and the point at ξ along the curved line of the bar element. The $\mathbf{e}_1$ is the unit tangent direction of the curved line at the point ξ and is derived as:

$$\mathbf{e}_1 = \{ e_{11} \ \ e_{12} \ \ e_{13} \}^T = \frac{1}{J} \{ \frac{\partial x}{\partial \xi} \ \ \frac{\partial y}{\partial \xi} \ \ \frac{\partial z}{\partial \xi} \}^T \qquad (2.5.5)$$

Where $J = \sqrt{\left(\frac{\partial x}{\partial \xi}\right)^2 + \left(\frac{\partial y}{\partial \xi}\right)^2 + \left(\frac{\partial z}{\partial \xi}\right)^2}$ is the Jacobian determinant of the co-ordinates transformation between the global co-ordinates x, y and z and the isoparametric co-ordinate ξ, e_{1j}, j=1,2,3 are the direction cosines.

The axial displacement increment at a point in the $\mathbf{e}_1$ direction can be obtained by projecting the displacement increments du, dv and dw in the x, y and z direction at the same point in this direction as following:

$$du_\xi = \{ e_{11} \ \ e_{12} \ \ e_{13} \} \{ du \ \ dv \ \ dw \}^T \qquad (2.5.6)$$

Where du_ξ is the axial displacement increment at a point within the element; T denotes transposition.

Combining the equation set (2.5.1) to (2.5.6), a relationship between the axial strain increment and the increments of the nodal displacement is obtained as following:

$$d\varepsilon = [\,B\,]\,\{\,dU\,\} \tag{2.5.7}$$

Where $\{\,dU\,\}=\{\,du_1 \;\; dv_1 \;\; dw_1 \;\ldots\; du_n \;\; dv_n \;\; dw_n\,\}^T$ is the vector of the nodal displacement increments. $[\,B\,]$ is the geometric matrix derived as follows:

$$[\,B\,] = \{\,e_{11} \;\; e_{12} \;\; e_{13}\,\}\,[\,F'\,]\,/\,J \tag{2.5.8}$$

$$[\,F'\,] = \begin{bmatrix} f_1' & 0 & 0 & f_2' & 0 & 0 & \ldots & f_n' & 0 & 0 \\ 0 & f_1' & 0 & 0 & f_2' & 0 & \ldots & 0 & f_n' & 0 \\ 0 & 0 & f_1' & 0 & 0 & f_2' & \ldots & 0 & 0 & f_n' \end{bmatrix} \tag{2.5.9}$$

Where $f_i' = \dfrac{\partial f_i}{\partial \xi}$, i = 1, ... n, are the derivatives of the shape function .

The steel reinforcement bar is assumed to be linearly elastic in the current research. So there is a linear constitutive equation for the axial strain increment and axial stress increment (the axial stress defined in the bar element is the axial force):

$$d\sigma = (\,EA\,)\;d\varepsilon \tag{2.5.10}$$

Where $d\sigma$ and $d\varepsilon$ are the axial stress increment and the axial strain increment; E and A are the Young's modulus of the steel bar and the area of the cross section of the bar respectively. The element stiffness matrix is derived as:

$$\begin{aligned} [\,K\,] &= \int_S (\,EA\,)\,[\,B\,]^T\,[\,B\,]\,ds \\ &= \int_{-1}^{1} (\,EA\,)\,[\,B\,]^T\,[\,B\,]\,J\,d\xi \end{aligned} \tag{2.5.11}$$

Where $[\,K\,]$ is the element stiffness matrix; S is the domain of the curved line of the bar element. Four curved bar elements with 2, 3, 4 and 5 nodes have been implemented into the program.

2.5.3 EXAMPLE ANALYSIS

Again, a few benchmark tests have been carried out before the program is used for three-dimensional analysis in this research. The first example is a curved bar over a quarter of a circle with radius r =10mm as shown in Figure 2.18. The bar is simply supported in the radial direction, fixed at one end and subjected to a tensile force of 100N at the other end as shown in the figure. The bar has constant axial stiffness *EA*. The problem is examined with 2-node, 3-node and 5-node bar elements. The results are given in Table 2.2.

The second example is almost the same as the first one except that it is with 7 nodes, as shown in Figure 2.19, instead of 9 nodes as in the first example. The problem is now examined with 2-node, 3-node and 4-node bar elements. The results are given in Table 2.3. From the results in these two tables, it is very clear that the elements have been properly implemented into the program and the accuracy is very good especially for the 3-node and 5-node bar elements.

Table 2.2 results of first example

No. of nodes per element	number of elements	number of Gauss points per element	axial stresses at Gauss points	analytical solution
2	8	1	100.48N	100N
3	4	2	100.00N 100.00N	100N
5	2	4	100.03N 99.98N 99.98N 100.03N	100N

Table 2.3 results of second example

No. of nodes per element	number of elements	number of Gauss points per element	axial stresses at Gauss points	analytical solution
2	6	1	100.86N	100N
3	3	2	100.01N 100.01N	100N
4	2	3	100.98N 98.82N 100.98N	100N

2.6 SOLUTION METHOD

In finite element analysis, solution procedures are usually based on incremental methods, that is, a problem is solved step by step with a small load increment within each step to secure solution accuracy and convergence:

$$[K_n] \{ dU_n \} = \{ dP_n \} \qquad n = 1, 2, \ldots N$$

$$\{ U_n \} = \{ U_{n-1} \} + \{ dU_n \} \qquad n = 1, 2, \ldots N \qquad (2.6.1)$$

Where N is total calculation steps; $[K_n]$ is overall stiffness matrix in the current calculation step n; $\{U_n\}$, $\{U_{n-1}\}$ and $\{ dU_n \}$ are the vector of the nodal displacements at end of step n, the vector of the nodal displacements at end of step n-1 and the increments of the nodal displacements within step n; $\{ dP_n \}$ is the vector of applied load increments in step n. The load increment $\{ dP_n \}$ may be different from step to step. In general, there is an unbalanced force (residual force) at end of each step. This unbalanced force may be added into the applied load increment in the next step, as discussed in later sections.

In this Section, a few commonly used solution methods, Euler method, modified Euler method and Newton-Raphson method, are reviewed briefly. Then a modified Newton-Raphson method is proposed and discussed in Section 2.6.3. Finally, a validating example is presented.

2.6.1 EULER AND MODIFIED EULER METHOD

A simple solution method is the Euler method in which the equation (2.6.1) is solved step by step and the unbalanced force at end of each step is ignored (Zienkiewicz 1977, Sloan 1981). The Euler method usually obtains a good convergent solution if the load increment in each step is very small. This means that convergence is slow using the Euler method.

To improve accuracy and convergence, a modified Euler method is proposed by Sloan (1981). In this modified Euler method, an unbalanced force is evaluated at the end of each step and is then applied in the next calculation step as a part of the applied load together with the applied load increment when solving the equation (2.6.1):

$$\{ P_n \} = \sum_{i=1}^{n} \{ dP_i \} \tag{2.6.2}$$

$$\{ R_n \} = \sum_{e} \iiint_{\Omega} [B]^T \{\sigma\} dV - \{ P_n \} \tag{2.6.3}$$

$$\{ dP^*_{n+1} \} = \{ dP_{n+1} \} + \{ R_n \} \tag{2.6.4}$$

Where $\{ P_n \}$ and $\{ R_n \}$ are the total applied force and the unbalanced force at end of step n; $\{ dP_i \}$ is the applied load increments in step i; Ω is the domain of element e and the summation is over all elements; $\{ dP_{n+1} \}$ and $\{ dP^*_{n+1} \}$ is the applied load increment and modified applied load increment including the unbalanced force from the previous step in step n+1. This modified Euler method is generally found to be stable and accurate (Sloan 1981, Burd 1986). Both the Euler method and the modified Euler method are available in FEPS.

2.6.2 NEWTON-RAPHSON METHOD

The Newton-Raphson method is another commonly used method for solving non-linear problems. In this method, if a solution at step n-1 has been obtained, the equation (2.6.1) at step n is solved by an iteration procedure to secure a zero (or almost zero) unbalanced force:

$$[K_n]^m \{dV_n\}^m - \{R_n\}^m = \{0\} \qquad m=1,2,3,\ldots$$

$$\{dU_n\}^{m+1} = \{dU_n\}^m + \{dV_n\}^m \qquad (2.6.5)$$

$$\{R_n\}^{m+1} = [K_n]^{m+1}\{dU_n\}^{m+1} - \{dP_n\}$$

Where $[K_n]^m$ is the overall stiffness matrix at iteration m within step n; $\{dV_n\}^m$ and $\{R_n\}^m$ are the displacement increments and the unbalanced force at iteration m within step n; $\{dU_n\}^m$ and $\{dU_n\}^{m+1}$ are the total displacement increments at the start and end of iteration m in step n; $\{dP_n\}$ is the applied load increments in step n. The calculation begins with initial values $\{dU_n\}^1 = \{0\}$ and $\{R_n\}^1 = \{dP_n\}$. The analysis proceeds to the next step when the unbalanced force $\{R_n\}^{m+1}$ satisfies a given convergent criterion:

$$|\{R_n\}^{m+1}| / |\{P_n\}| < \delta_1 \quad \text{for relative error}$$

or $$|\{R_n\}^{m+1}| < \delta_2 \quad \text{for absolute error} \qquad (2.6.6)$$

Where $\{P_n\}$ is the total applied load by end of step n; δ_1 and δ_2 are two very small given numbers to control solution accuracy.

In the Newton-Raphson method, the overall stiffness matrix $[K_n]^m$ is updated not only for each step but also for each iteration within a step. This will increase computing time. A variant version of the Newton-Raphson method is usually used in which the overall stiffness matrix is updated in each step instead of in each iteration. For simplicity, this variant version is referred as Newton-Raphson method in this research.

2.6.3 MODIFIED NEWTON-RAPHSON METHOD AND INITIAL STIFFNESS METHOD

To improve accuracy, convergence and efficiency of the Newton-Raphson method, a modified Newton-Raphson method is proposed in this research. In the modified formulation, a maximum number of iterations is set up for each step, that is, the iteration in a step will stop when the unbalanced force satisfies a given convergent criterion as shown in equation (2.6.6)

or when the iteration number reaches the given maximum number. The unbalanced force at the end of each step, if any, is then added into the next step as a part of the applied load as in equation (2.6.4) in the modified Euler method. Moreover, the overall stiffness matrix [K] is updated only when the unbalanced force at end of a step is larger than a given value:

$$| \{ R_n \}^{m+1} | / | \{ P_n \} | > \delta_3 \qquad \text{for relative error}$$

$$\text{or} \qquad | \{ R_n \}^{m+1} | > \delta_4 \qquad \text{for absolute error} \qquad (2.6.7)$$

Where δ_3 and δ_4 are two given small numbers.

Another common solution method available in the program is a variant version of the initial stiffness method (for simplicity, it is referred to as initial stiffness method in this project). In this method, the initial elastic overall stiffness matrix [K_0] is used throughout the calculation. As in the modified Newton-Raphson method, a maximum iteration number is set up for each step and the unbalanced force at end of each step is added into next step as a part of the applied load.

From the discussion above, it is clear that if the maximum iteration number is set to 1, and δ_3 and δ_4 in equation (2.6.7) are set to zero, the modified Newton-Raphson method becomes the modified Euler method discussed in Section 2.6.1. If δ_3 and δ_4 are set to very large numbers, the modified Newton-Raphson method becomes the initial stiffness method. When the maximum iteration number is set to a very large number with δ_3 and δ_4 set to zero, the modified Newton-Raphson method becomes the Newton-Raphson method (the stiffness matrix is updated in each step). This means that the initial stiffness method, the modified Euler method, and the Newton-Raphson method can all be treated to be an alternative version of the modified Newton-Raphson method.

2.6.4 EXAMPLE ANALYSIS

The example for the modified Matsuoka model in Section 2.4.3 is used here to verify the program after the implementation of the solution methods. The calculation is carried out with the Modified Euler method, the Newton-Raphson method, the modified Newton-Raphson method and the initial stiffness method respectively. All the solution methods give the same results as shown in Figure 2.15. This means that the solution methods are successfully implemented and work properly. For this example, the computing time with the modified Newton-Raphson method and the initial stiffness method is less than those with the modified Euler method and the Newton-Raphson method. To obtain a stable solution, the Newton-Raphson method needs more calculation steps than the other three. However, elastic-plastic problems are complex and the best solution method is usually problem dependent (Zienkiewicz 1977). A detailed evaluation of different solution methods is not the task of this research. In this project, the initial stiffness and the modified Newton-Raphson method seem more stable in the analysis with an interface in Chapter 5.

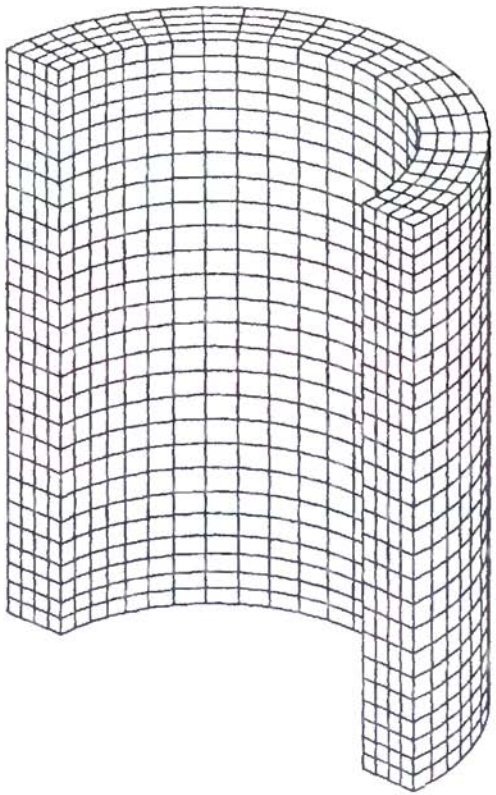

Figure 2.1 A pipe mesh generated by DATAIN

```
! 3D mesh of a pipe
A, 3,   75.,    0.,    0.,
%, 5, 6.25,     0.,    0.,
%, 5,    0.,   5.5,    0.,
%,-2,    0.,   7.0,    0.,
%,-12,   0.,   9.0,    0.,
%,-2,    0.,   7.0,    0.,
%,-4,    0.,   5.5,    0.,
%, 3,    0.,   0.0,   6.5,
%,-2,    0.,   0.0,   7.5,
%,-2,    0.,   0.0,   9.0,
%,-14,   0.,   0.0,   10.,
%,-2,    0.,   0.0,   9.0,
%,-2,    0.,   0.0,   7.5,
%,-2,    0.,   0.0,   6.5,
E,

A, 8,    1 ,   2 ,    7,    6,
       126,  127,  132,  131,
%,  4,   *, 8,    1,
%, 24,   *, 8,    5,
%, 26,   *, 8,  125,
E,
E,
```

Table 2.1 Input data of DATAIN for a pipe mesh

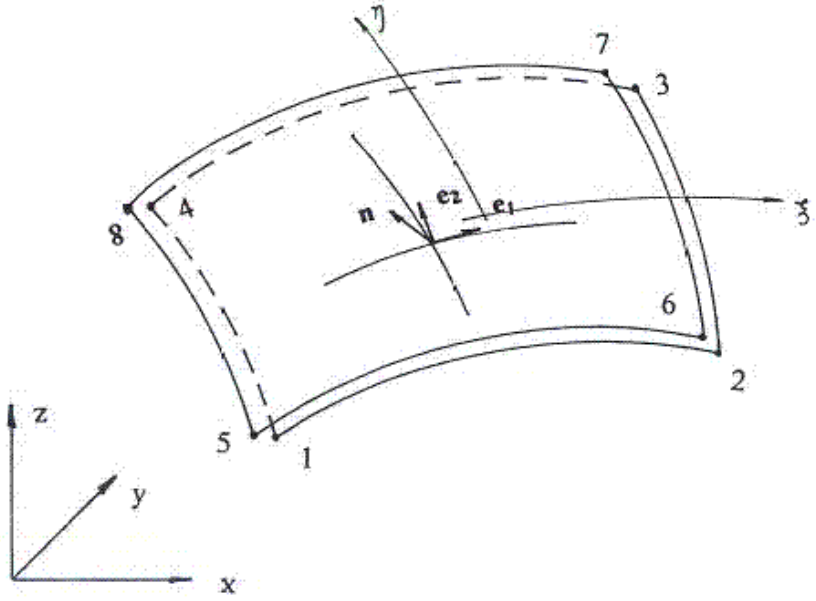

Figure 2.2 A quadrilateral interface element

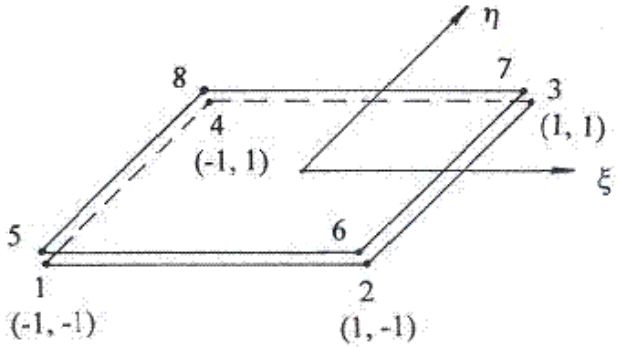

Figure 2.3 Interface element on an isoparametric plane

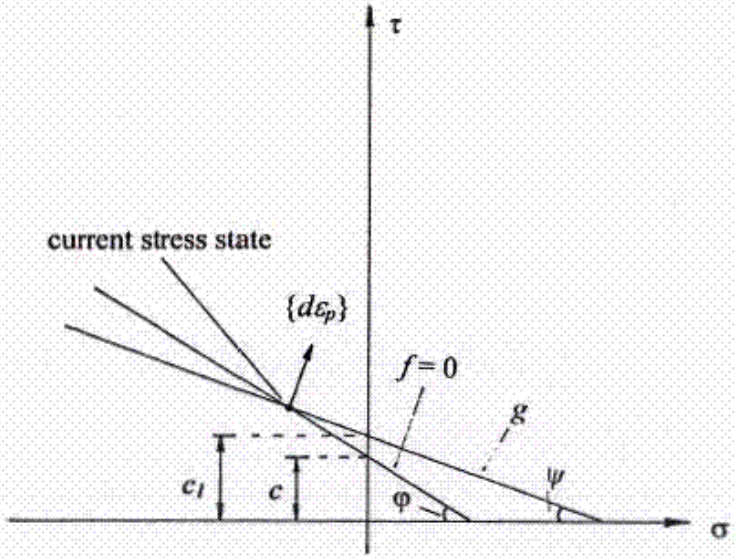

Figure 2.4 Mohr-Coulomb interface model

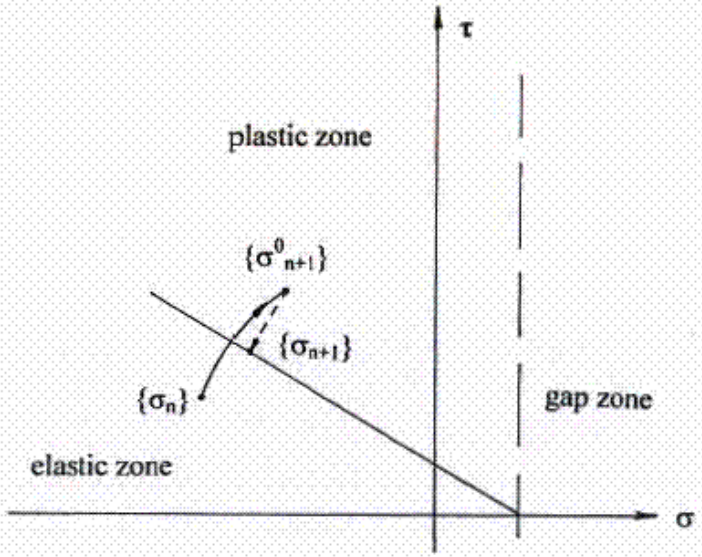

Figure 2.5 Different stress regions in interface model

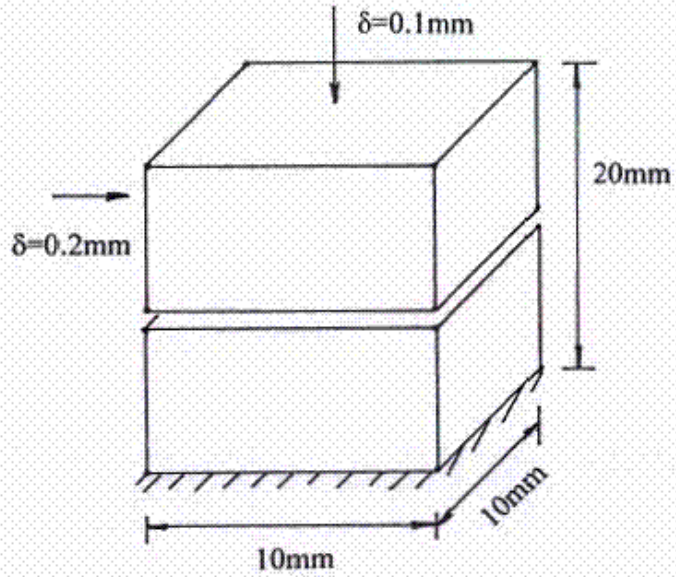

Figure 2.6 An example of interface

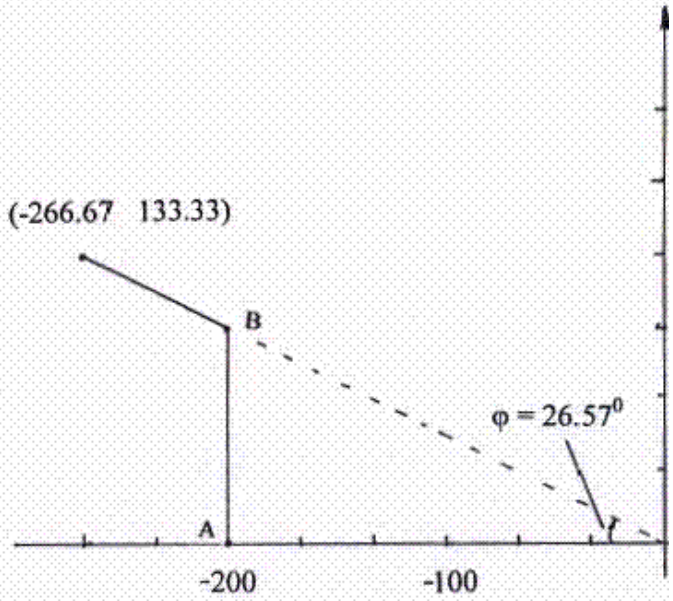

Figure 2.7 Yield behaviour of interface

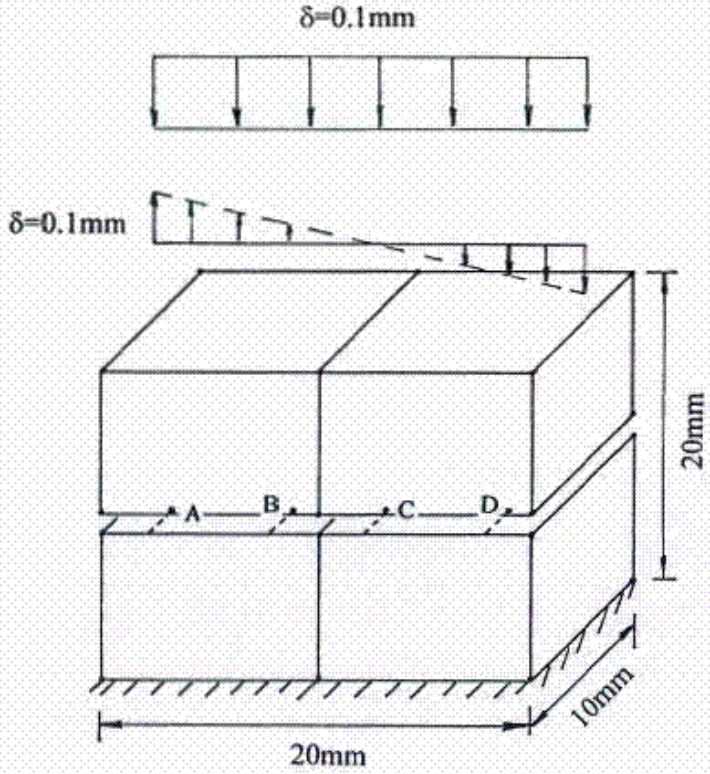

Figure 2.8 An interface with gap

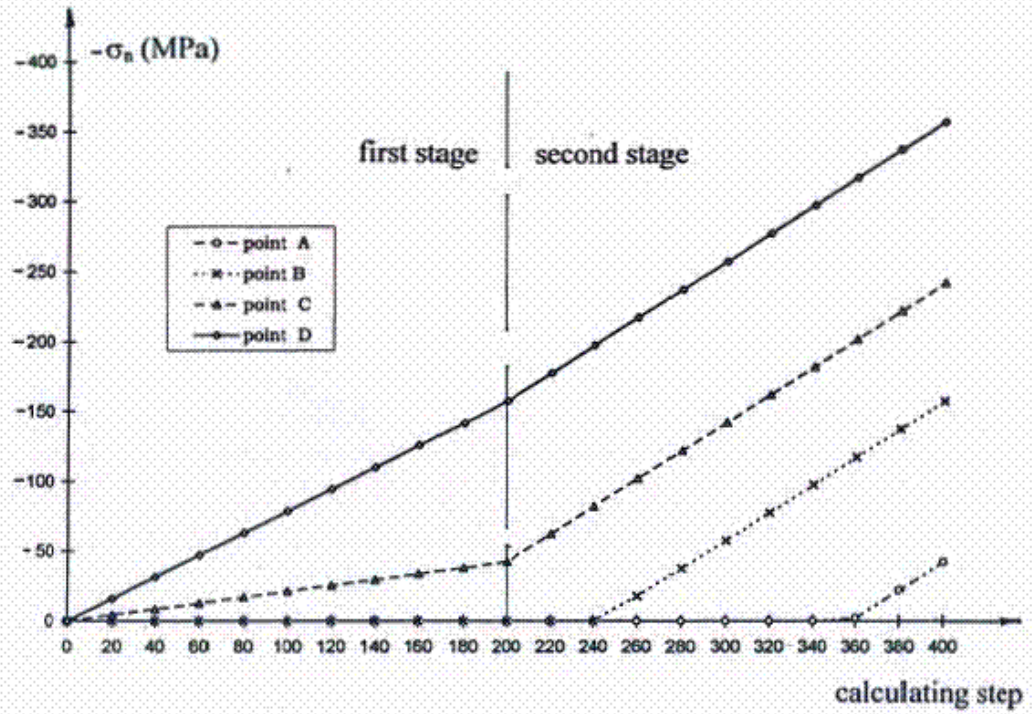

Figure 2.9 Gap behaviour of interface

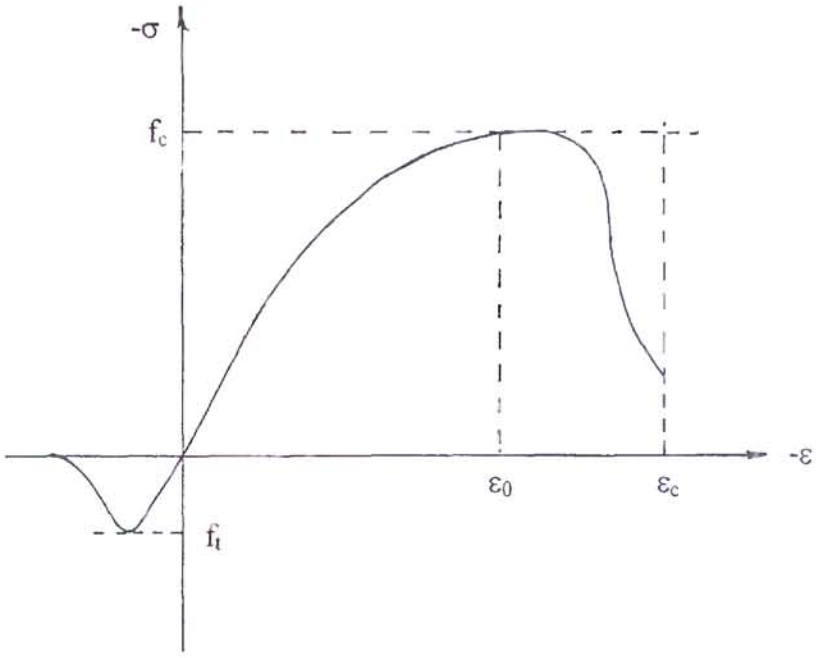

Figure 2.10 A typical uniaxial stress-strain curve for concrete (from Bangash 1989)

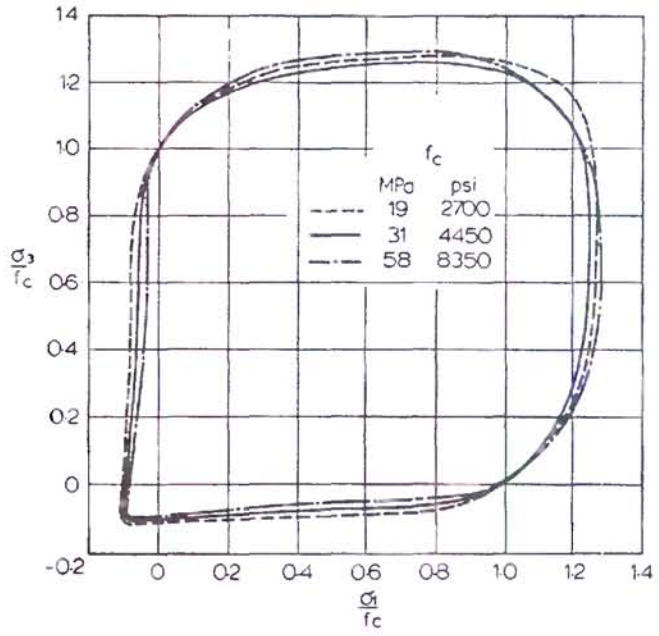

Figure 2.11 A typical biaxial stress interaction in concrete model (from Neville 1981)

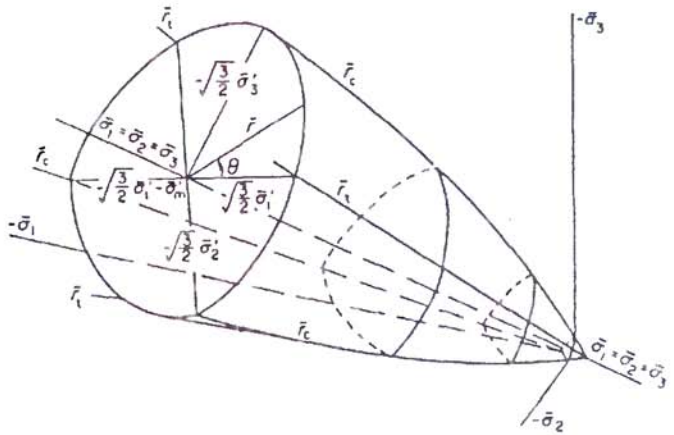

Figure 2.12 A typical three-dimensional concrete model (from Boswell and Chen 1987)

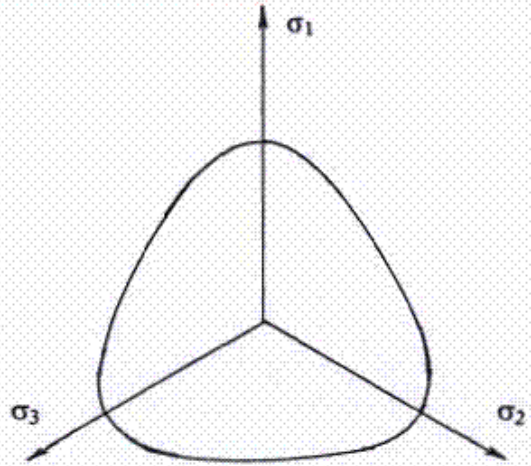

(a) Yield surface

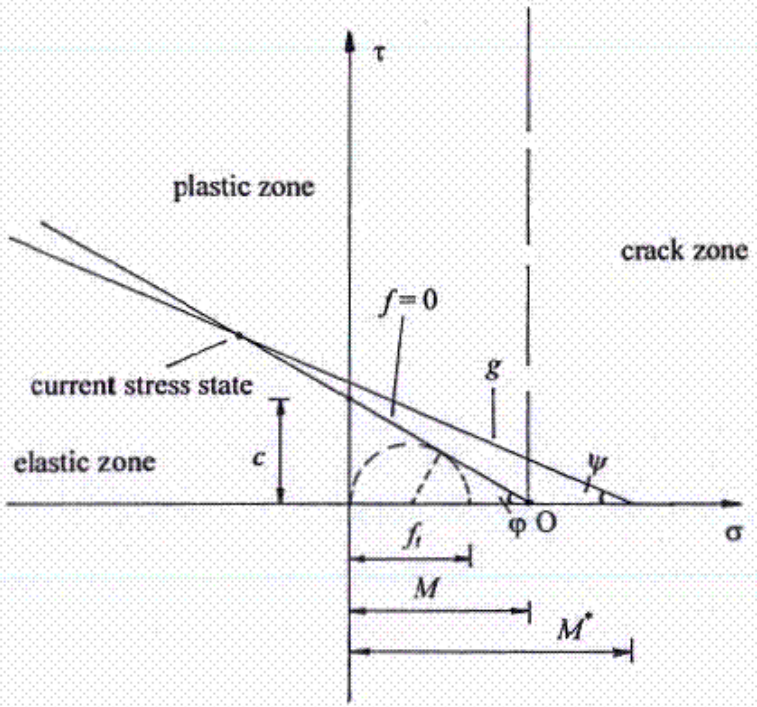

(b) Relationship between c, f_t, M and M^*

Figure 2.13 Modified Matsuoka model

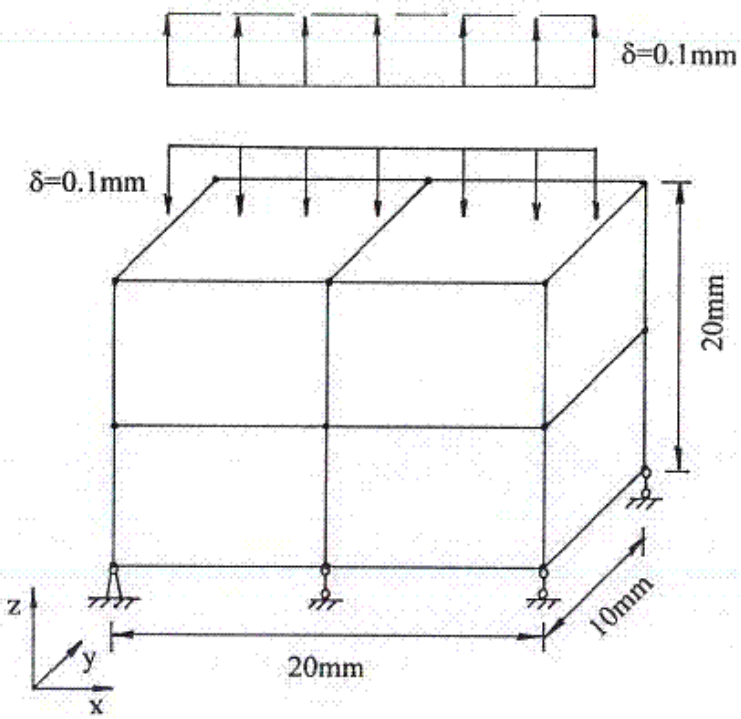

Figure 2.14 An example for modified Matsuoka model

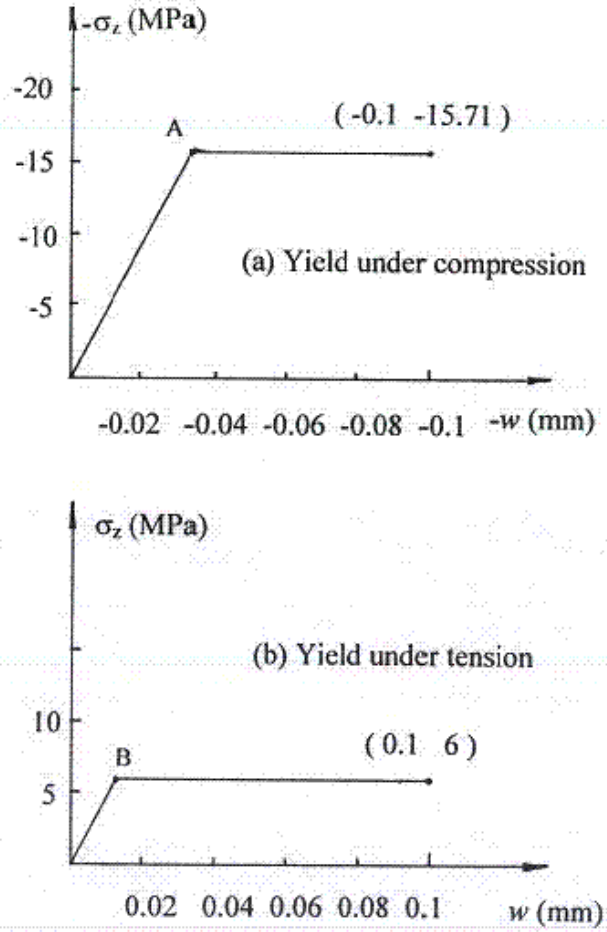

Figure 2.15 Stress yield behaviour in modified Matsuoka model

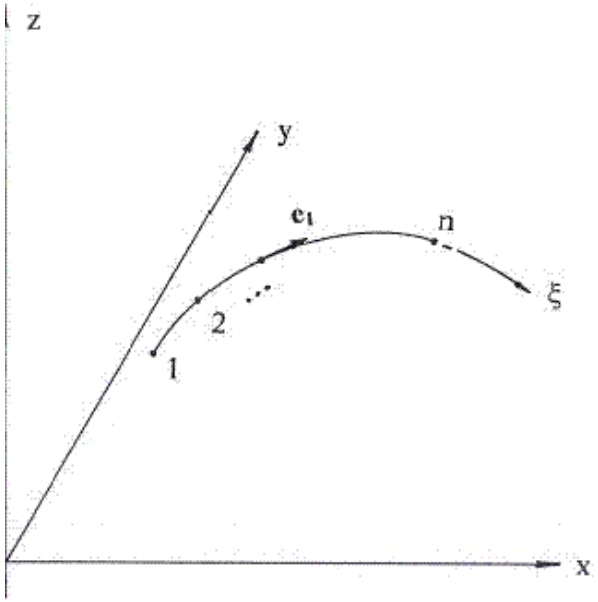

Figure 2.16 Curved bar element



Figure 2.17 Bar element on an isoparametric plane

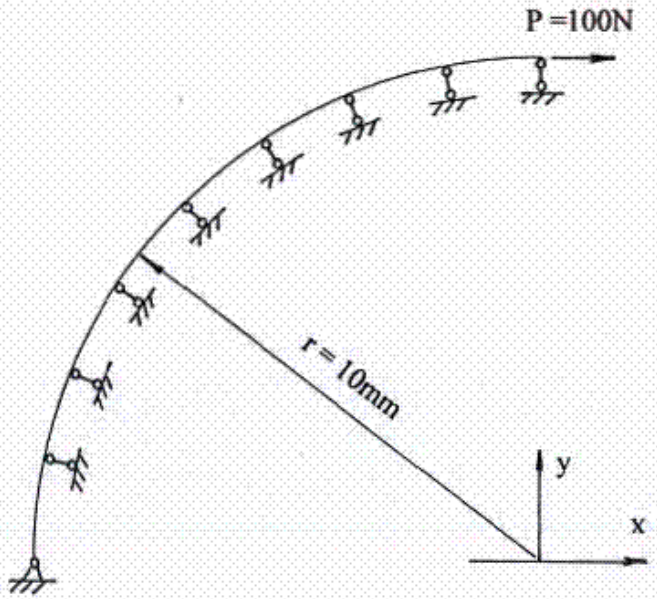

Figure 2.18 First example for bar element

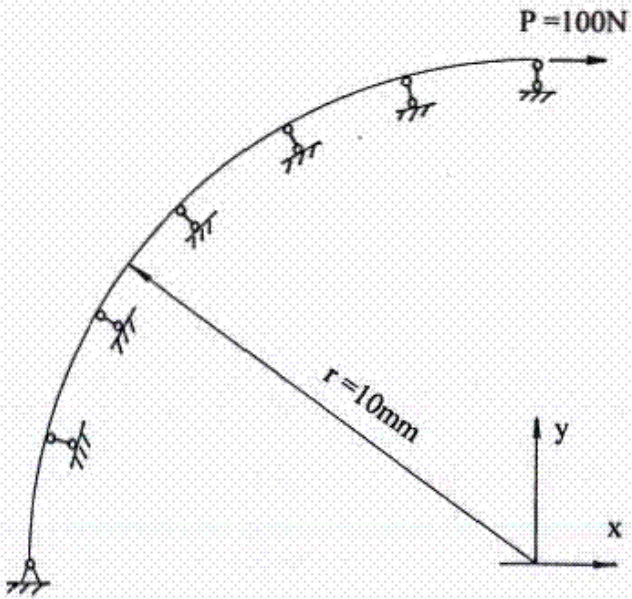

Figure 2.19 Second example for bar element